

Figure S1. Biochemical Experiments that Characterize the Free RP or the 26S, Related to Figure 1

(A) SDS-PAGE gel of purified human p28-RP complex.

(B) The free RP was purified and characterized through FPLC as described in the methods section.

(C) Different fractions from FPLC have been collected and detected by native gel. As illustrated in the gel, most 26S can be separated out from the RP and only fraction 22 and 23 have been applied for the further biological experiments.

(D) SDS-PAGE gel was utilized to characterize the purified free RP. To give better insight of the biological composition of the free RP, the bands with faster mobility, marked with the rectangles, have been further analyzed by mass spectrometry (MS). The existence of p28 and Rpn12 was detected, which is consistent with the cryo-EM structure data.

(E) Western blot assay of purified RP and cell lysate with the anti-PAAF1 antibody.

(F) With the Malachite Green assay, the ATPase activity of the RP and 26S was detected. The ATPase activities of RP and 26S proteasome calculated were about 45 and 24 ATP/min, respectively.

(G) Coomassie blue staining of SDS-PAGE gel of yeast RP and 26S complexes, and native gel (right) of yeast RP.

(H) Deubiquitylation by the free RP is independent of ATP hydrolysis. Purified free RP (Ubp6-free) from yeast was mixed with ubiquitylated pySic1-iRFP at $t=0$ in the presence of indicated nucleotide. Samples were analyzed by western blot.

(I) Ubiquitylated GFP-pySic1 (left) or pySic1-GFP (right) was mixed with purified human 26S proteasome (Usp14-free) at $t = 0$. Samples were analyzed by western blot.

(J) pySic1-GFP is not degraded efficiently by 26S proteasome. Ubiquitylated pySic1-GFP was mixed with purified yeast 26S proteasome (Ubp6-free) at various concentrations at $t = 0$. Fluorescence intensity from GFP was monitored continuously in a fluorometer at room temperature. Maximal intensity reduction (ΔSub ; Left), converted to equivalent substrate concentration, was plotted with the proteasome concentrations, suggesting lack of enzyme turnover.

(K) The rate of substrate degradation by the 26S proteasome (left) and the rate of deubiquitylation by the RP (right) were measured by quantifying the intensity corresponding to substrate with 10~15 ubiquitins.

(L) Degradation of ubiquitylated pySic1-iRFP by purified human 26S proteasome (Usp14-free).

(M) Rates of substrate processing by 26S proteasome and RP. Purified 26S and RP (Ubp6-free) at various concentrations from yeast was mixed with ubiquitylated pySic1-iRFP in a buffer containing ATP. Samples were analyzed by western blot.

(N) GroEL trap does not affect normal substrate degradation. GroEL-D87K was added at indicated concentration to degradation assay of ubiquitylated pySic1-iRFP by purified yeast 26S proteasome (Ubp6-free). Samples were analyzed by western blot.

(O) Ubiquitylated iRFP as a fluorescent reporter for proteasomal activity. 500nM Sic1- iRFP was ubiquitylated, purified and mixed with the 26S proteasome from yeast as described in the methods. Fluorescent intensity of the reporter was continuously monitored in a fluorescence spectrophotometer at room temperature.

(P) Free RP lacks ATP-dependent unfolding activity. 500nM ubiquitylated Sic1-iRFP was mixed with the RP from yeast, in the presence or absence of the GroEL trap as described in methods. As a positive control, Sic1-iRFP carrying a C-terminal *ssrA* sequence (*ssrA*) was incubated with purified ClpA unfoldase. In contrast to the fluorescence loss due to proteasome-induced unfolding and translocation of the *ssrA*-fused iRFP, we did not observe any fluorescence signal change of ubiquitylated Sic1-iRFP, in the presence of the free RP and excess GroEL. This result confirmed that the p28-bound RP is deficient in substrate unfolding.

(Q) Native gel examining the assembly of purified p28-RP and CP into 26S proteasome. After the reconstitution process, the bands of free RP disappeared while the bands of 26S proteasome showed up. The fifth lane shows the reconstitution result by mixing 1.0 μg RP with 0.5 μg CP. The sixth lane shows the reconstitution result by mixing 1.0 μg RP with 2.5 μg CP.

(R) 0.2 μg RP and 0.1 μg CP were reconstituted to 26S in a volume of 10 μL . Then 1 μL $\sim 8 \mu\text{M}$ Ub-Sic1 was introduced for the further degradation test.

(S) Western blot of the native gel with an anti-p28 antibody was used to detect the dissociation of p28 after *in vitro* reconstitution of 26S from purified RP and CP. Before the reconstitution, p28 was mostly bound to the purified RP (the 2nd lane). After the reconstruction, p28 was dissociated from RP and no p28 was detected to attach to the reconstituted 26S (the 4th lane). There was a small amount of free RP remaining in the reconstituted solution.

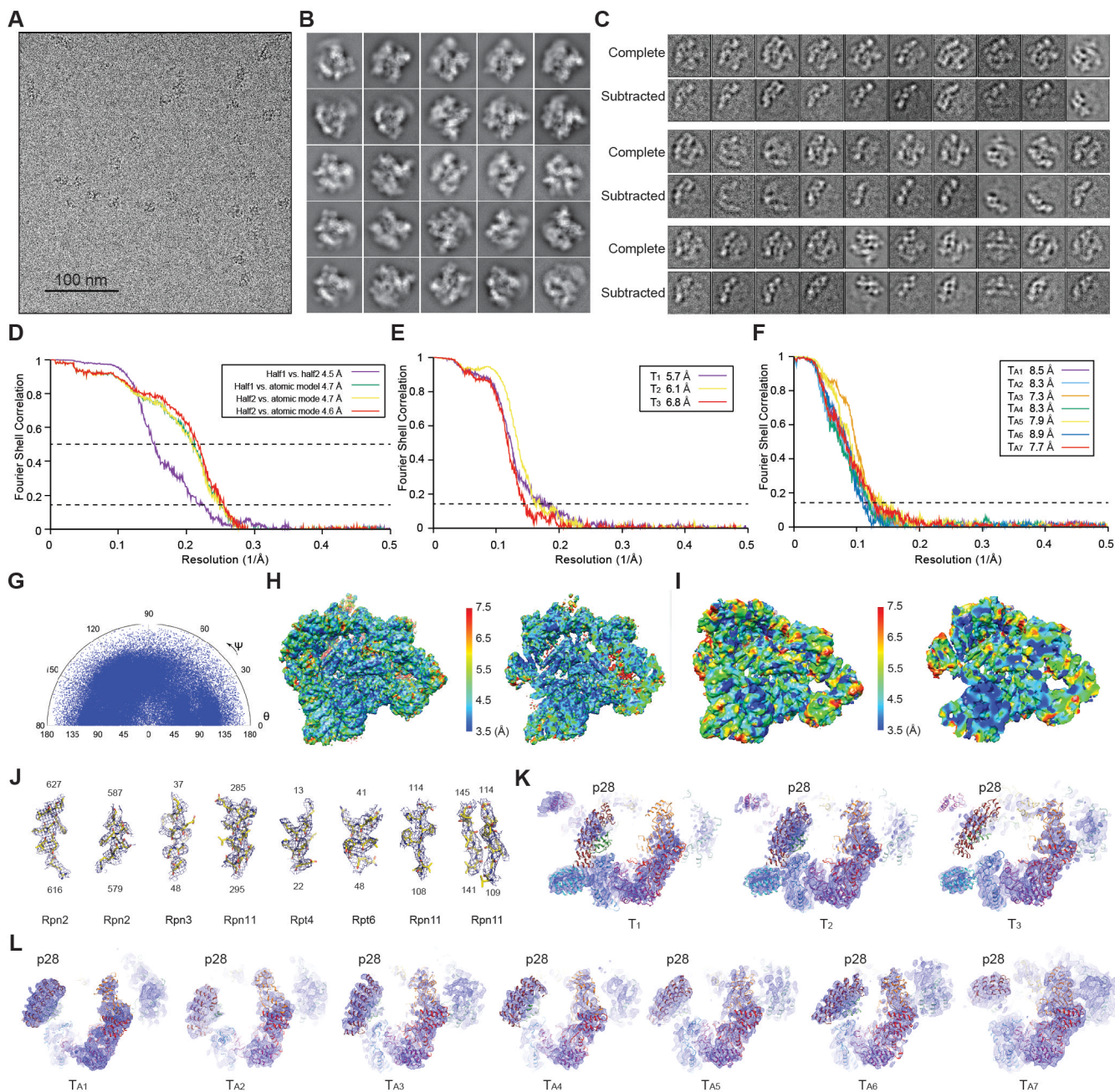


Figure S2. Cryo-EM Structural Determination, Related to Figure 1

(A) Typical cryo-EM micrograph showing the transmission projections of the free human p28-RP.

(B) A gallery of representative reference-free class averages of the free human p28-RP.

(C) Comparison of reference-free class averages from the complex free RP in T₁/T₂/T₃ (the 1st, 3rd and 5th rows) with those from the particle images whose non-AAA components were subtracted (the 2nd, 4th and 6th rows).

- (D) FSC plots give an estimate of the resolution of the free RP map from the 117,471-particle dataset. Black curve shows the gold-standard FSC of the free RP reconstruction. Orange, green and cyan curves show the FSC cross-validation using the atomic model refined against the two half-maps and the merged map refined with 117,471-particle dataset.
- (E) Gold-standard FSC plots of the T₁, T₂ and T₃ maps.
- (F) Gold-standard FSC plots of the Rpn1-p28-AAA subcomplex in the T_{A1-7} states.
- (G) Angular distribution of single particle images used for the refined 4.5 Å map.
- (H) Local resolution of the refined free RP map computed by ResMap using the two half maps refined separately in a gold-standard procedure.
- (I) Local resolution of the refined free RP map computed by Bsoft by local FSC between the refined map and the refined atomic model.
- (J) The atomic models of representative secondary structures, shown as a stick representation, are superimposed with the corresponding high-resolution cryo-EM densities shown in blue meshes.
- (K) The density maps of the AAA domains of the ATPase in the T₁, T₂ and T₃ states are shown in blue meshes and superimposed with corresponding pseudo-atomic models in a cartoon representation.
- (L) The density maps of the AAA domains of the ATPase in the T_{A1-7} states. The features in the densities of the AAA domains and the assembly chaperone p28 are improved in the T_{A1-7} states as compared to those in the T₁₋₃ states.

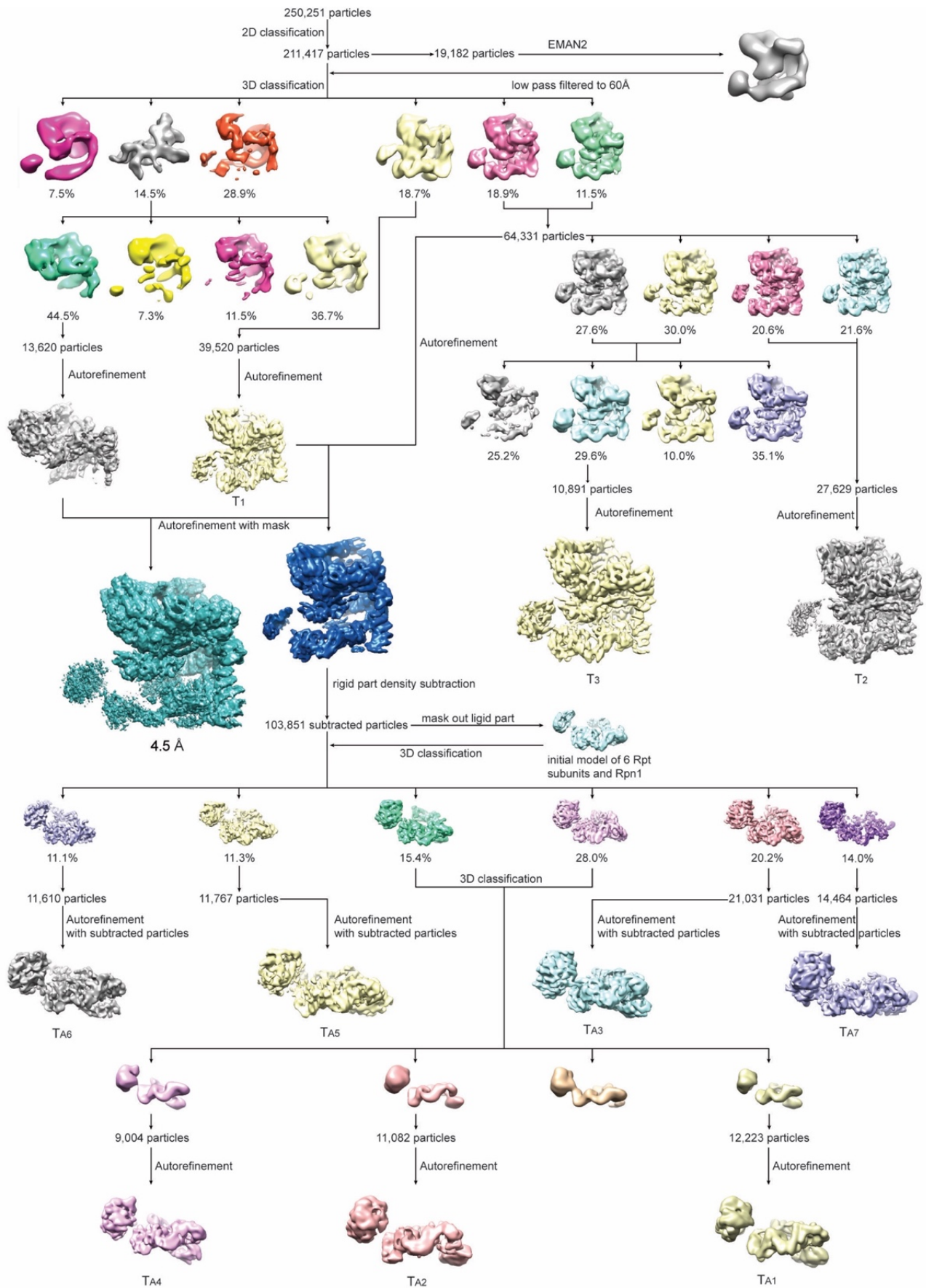


Figure S3. 3D Classification of the Cryo-EM Dataset, Related to Figure 1

Schematic procedure of the maximum-likelihood based 2D and 3D classification that helped to improve the homogeneity of the particle dataset. For the reconstruction and refinement of the seven microstates of Rpn1-p28-AAA subcomplex, the non-AAA-subtracted particle images were used.

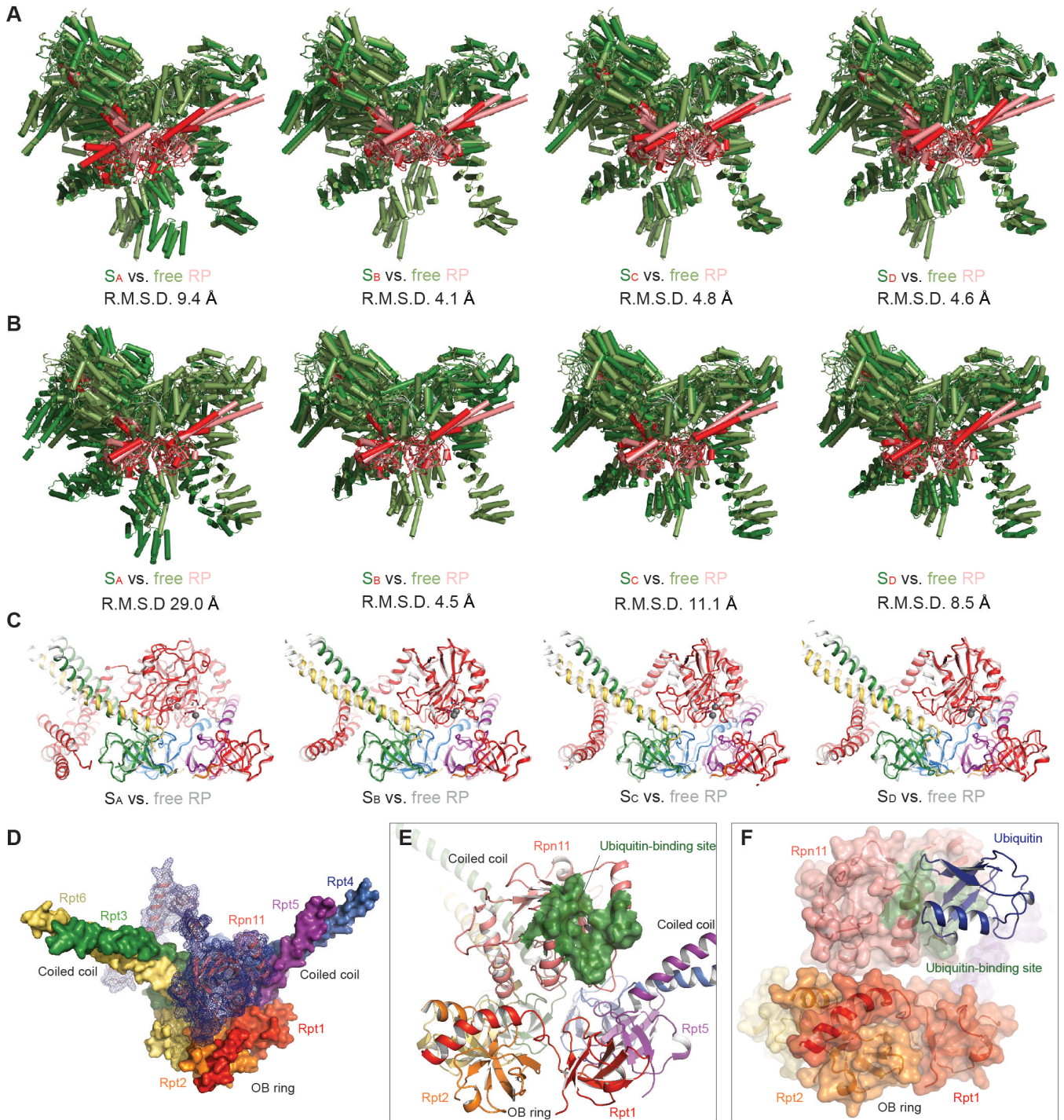


Figure S4. Comparison of the Non-AAA Subcomplex with Those in the Four Conformational States of 26S Proteasome, Related to Figure 3

(A) Structural comparison of the non-AAA subcomplex model with that of the human 26S proteasome in the S_A , S_B , S_C and S_D state, when they are aligned against the lid. The lid and the CC-OB ring of the non-AAA subcomplex in the free RP are colored light green and pink.

- (B) Structural comparison of the non-AAA subcomplex model with that of the human 26S proteasome in the S_A, S_B, S_C and S_D state, when they are aligned against the CC-OB ring. The lid and the CC-OB ring of the non-AAA subcomplex in the free RP are colored light green and pink.
- (C) Structural comparison of the Rpn11-OB model of the free RP with that of the human 26S proteasome in the S_A, S_B, S_C and S_D state, when they are aligned against the CC-OB ring.
- (D) Close-up view of Rpn11 interacting with the CC-OB domain of ATPase hetero-hexamers in the free RP structure. The MPN domain of Rpn11 sits right above the entrance of the OB ring, effectively blocking the OB channel. The C-terminal helices encircle half of the circumference of the CC domain of Rpt3-Rpt6 dimer.
- (E) The putative site of ubiquitin binding on the Rpn11 surface, highlighted by green surface representation superposed on the cartoon representation for the rest of the structure.
- (F) Ubiquitin is docked onto the Rpn11 surface, showing that the ubiquitin-binding site is well accessible, but that the substrate is left outside of the OB ring.

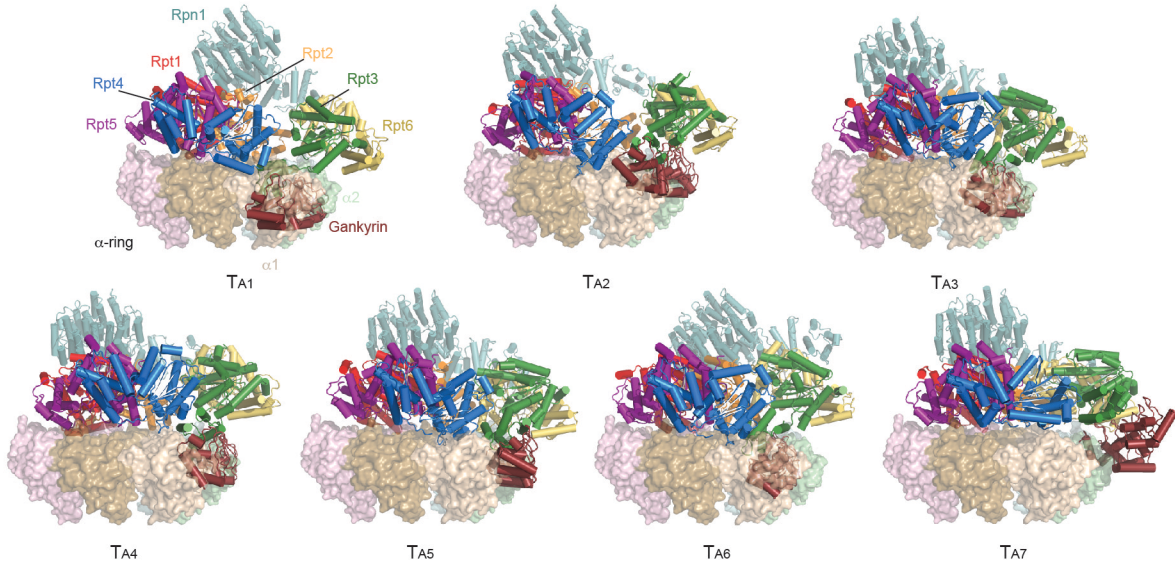
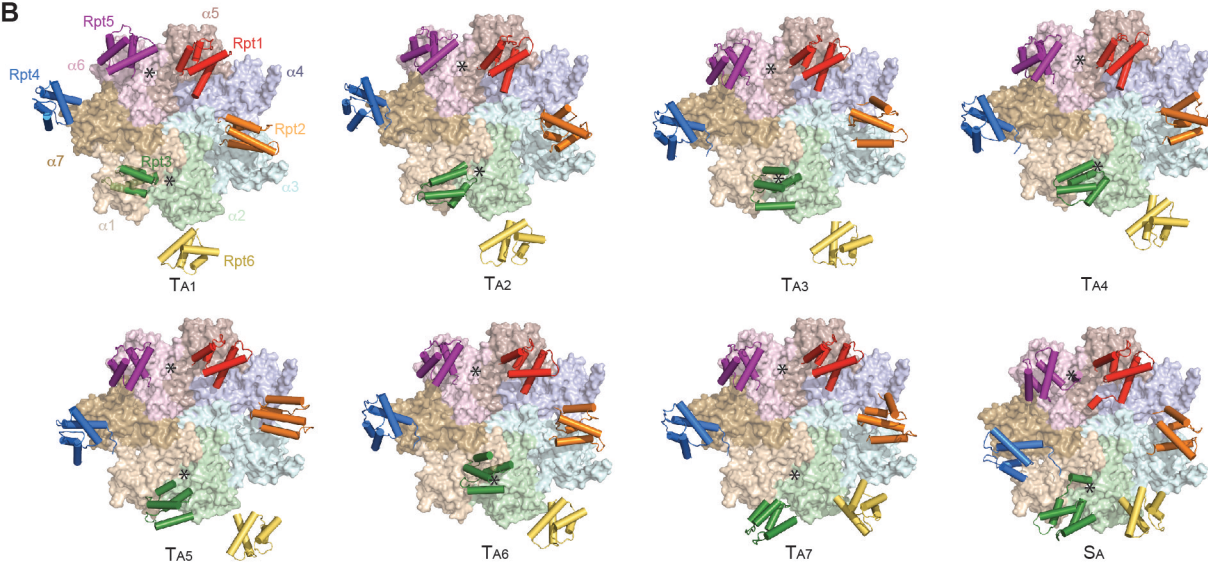
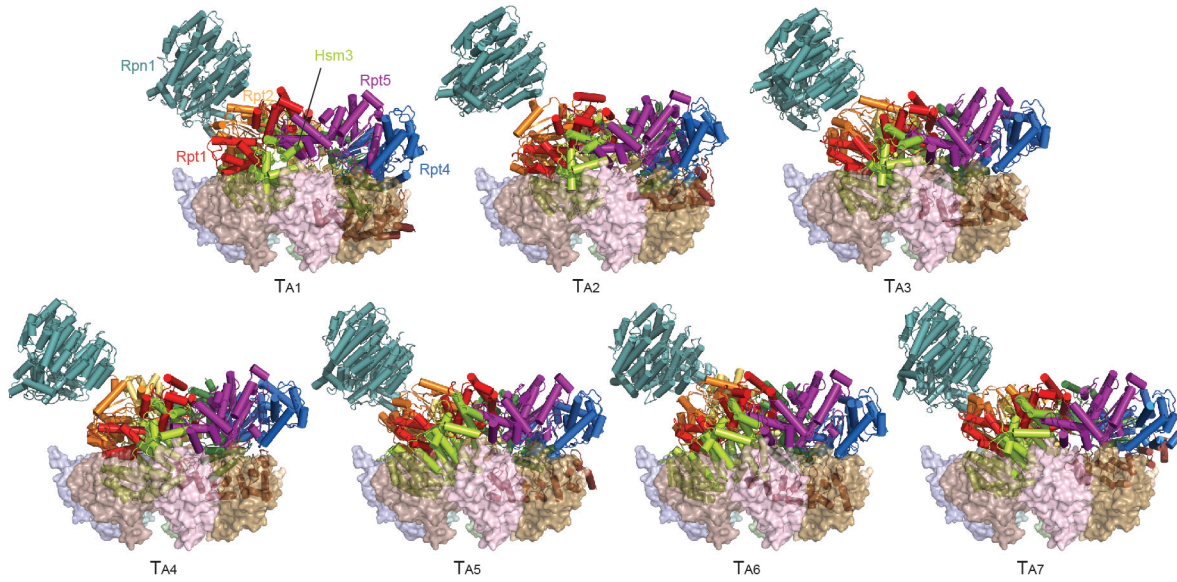
A**B****C**

Figure S5. Docking of the Rpn1-p28-AAA Subcomplex on the CP, Related to Figure 5

(A) Side view of the p28-AAA subcomplex in the seven microstates docked onto the α -ring surface, by aligning the AAA domains in the free RP against those in the 26S in the S_A state.

(B) Estimation of the distances between Rpt C-termini and the α -pockets through docking of the p28-AAA subcomplex in the seven microstates onto the α -ring surface, using the same alignment as shown in (A). Asterisks label the $\alpha 1$ - $\alpha 2$ and $\alpha 5$ - $\alpha 6$ pockets, where in the S_A state of assembled proteasome holoenzyme the Rpt3 and Rpt5 C-terminal HbYX motifs are inserted.

(C) Hsm3 docked onto the Rpt1 C terminus, showing the major clash with the α -ring of CP in the seven microstates.

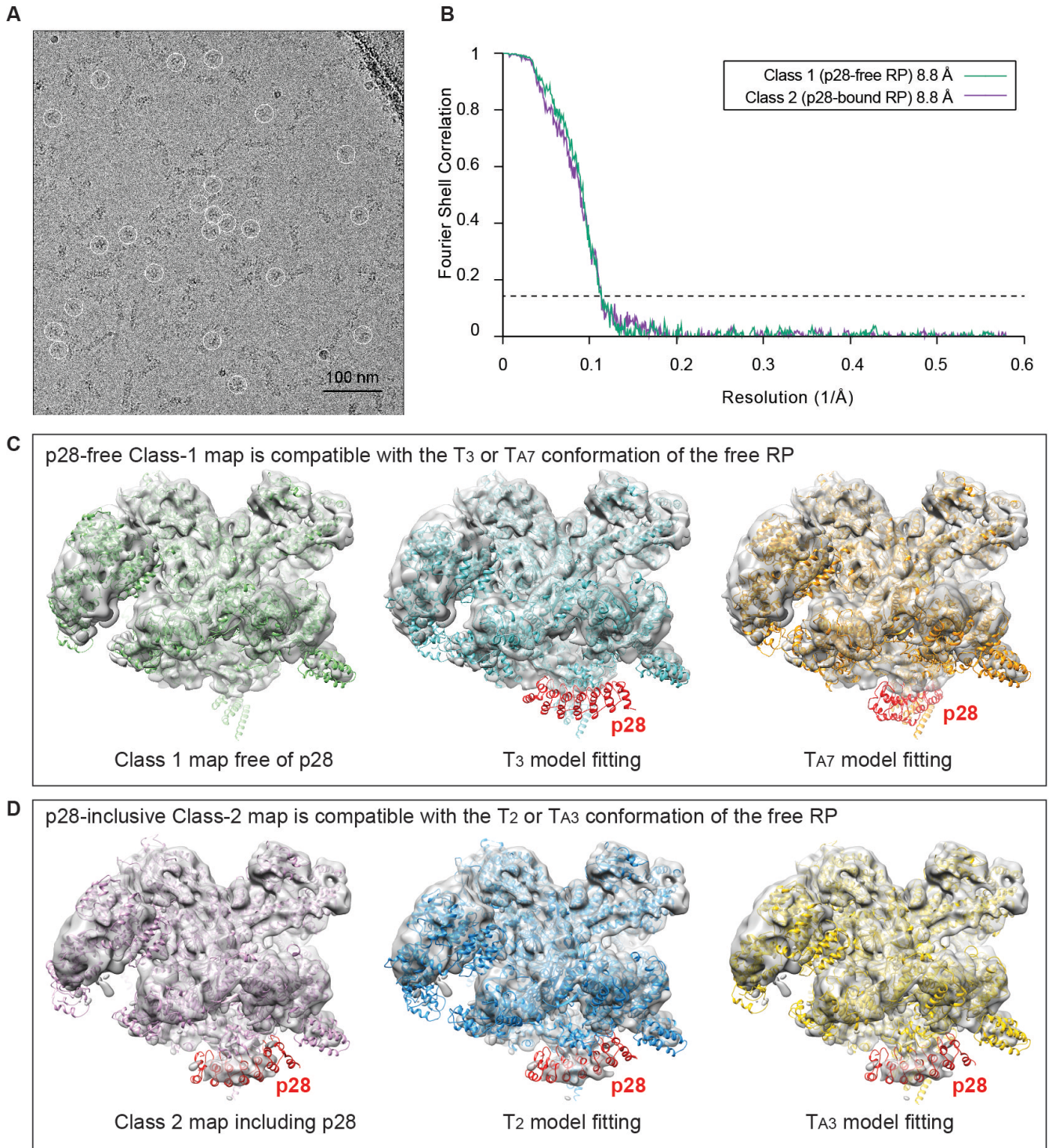


Figure S6. Structural Determination of p28-Free RP from a Purified 26S Dataset, Related to Figure 6

(A) Particle-picking of free RP from a typical cryo-EM micrograph imaged from samples of purified human 26S. The free RP are supposed to yield during cryo-plunging procedure, as the air-water interface may dissociate the RP from the CP.

(B) Gold-standard FSC curves of the two reconstructions from this dataset gave an estimate of resolution in the p28-free RP density map.

(C) The cryo-EM density map of the p28-free RP from class 1 is interpreted with pseudo-atomic model colored in green (left), fitted with the hybrid model of the T_3 state of p28-bound RP (middle), and fitted with the hybrid model of the T_{A7} state of p28-bound RP (right). The atomic model of p28 is colored red.

(C) The cryo-EM density map of the p28-bound RP from class 2 is interpreted with pseudo-atomic model colored in purple (left), fitted with the hybrid model of the T_2 state of p28-bound RP (middle), and fitted with the hybrid model of the T_{A3} state of p28-bound RP (right). The atomic model of p28 is colored red.

Table S1. Root-Mean-Square Deviation (R.M.S.D.) between the Rpn1-p28-AAA States (T_{A1-7}) and the Holoenzyme S_A State, Related to Figure 5.

	T_{A2}	T_{A3}	T_{A4}	T_{A5}	T_{A6}	T_{A7}	S_A
T_{A1}	17.7	17.3	20.0	17.1	16.3	22.7	41.4
T_{A2}		11.9	11.1	16.8	19.9	17.6	30.7
T_{A3}			9.0	11.0	15.4	15.4	30.1
T_{A4}				12.8	16.2	14.5	30.7
T_{A5}					12.5	12.8	37.2
T_{A6}						18.9	40.1
T_{A7}							30.5

Table S2. Inter-Subunit Interfacial Areas in Rpn1-p28-AAA States (T_{A1-7}) and S_A State, Related to Figure 5. In the table, ‘NA’ (Not Available) means that the subunit pair is not in contact.

	T_{A1}	T_{A2}	T_{A3}	T_{A4}	T_{A5}	T_{A6}	T_{A7}	S_A
Rpt1-Rpt2	1420	1487	937	1265	1092	670	1148	2011
Rpt2-Rpt6	NA	15	62	21	NA	575	692	1869
Rpt6-Rpt3	1405	1125	1081	1567	1313	1378	1735	1125
Rpt3-Rpt4	304	260	144	212	182	388	90	1958
Rpt4-Rpt5	2452	2208	1590	1791	1777	1726	1744	2140
Rpt5-Rpt1	725	879	896	955	1035	865	720	1989
Rpn1-Rpt2	194	428	595	363	387	495	267	361
p28-Rpt3	1813	2329	1404	1619	1310	905	879	NA
p28-Rpt4	26	222	153	6	NA	NA	NA	NA